Basin-scale internal wave dynamics during a winter cooling period in a large lake

Francisco J. Rueda, S. Geoffrey Schladow, and Sveinn Ó. Pálmarsson
Department of Civil and Environmental Engineering, University of California, Davis, California, USA

Received 27 April 2001; revised 17 December 2001; accepted 3 April 2002; published 27 March 2003.

[1] Basin-scale internal waves are examined using a combined field observation and 3-D numerical approach. The field site, Lake Tahoe (CA-NV) during winter, is characterized by the presence of a weak density stratification and the passage of several storm fronts of varying character. Under these conditions internal waves with periods greater than 5 days and displacements of 30 m are possible. The model used is shown to have negligible numerical dissipation and sufficiently small phase lag over the time periods needed to represent basin-scale waves. Both the numerical results and the observations identify the presence of three Kelvin modes and one Poincaré mode. While the wave periods are consistent with theoretical predictions, the spatial characteristics are far more complex than theory can predict. The spatial features are revealed through analysis of the integrated potential and kinetic energy fields yielded by the model. This shows that the basin topography exerts an influence on both Kelvin and Poincaré waves. The effect of the variable storms and, in particular, the phasing of the storms with respect to the internal waves is shown to be responsible for the amplification and annihilation of the basin-scale waves. *INDEX TERMS:* 1845 Hydrology: Limnology; 4255 Oceanography: General: Numerical modeling; 4544 Oceanography: Physical: Internal and inertial waves; *KEYWORDS:* internal waves, numerical modeling, observations, Lake Tahoe, wind-wave phase interaction, cooling

Citation: Rueda, F. J., S. G. Schladow, and S. Ó. Pálmarsson, Basin-scale internal wave dynamics during a winter cooling period in a large lake, *J. Geophys. Res.*, *108*(C3), 3097, doi:10.1029/2001JC000942, 2003.

1. Introduction

[2] Lake Tahoe (Figure 1) is located along the crest of the Sierra Nevada mountain range, between California and Nevada at an altitude of 1898 m. It has a maximum depth of 505 m, and an average depth of 313 m. Its surface area is 501 km^2, and that of the watershed is 812 km^2. The lake contains 156 km^3 of water, with a hydraulic residence time of approximately 650 years. The watershed's geology, large volume, and limited drainage area are largely responsible for the lake's sparse algal population and clear waters [Goldman 1988]. Few nutrients are naturally available to fertilize its waters. However, human development in the Tahoe Basin over the last five decades has been damaging to the lake. The lake has responded to increased nutrient and particulate loading from the streams, atmosphere and groundwater with steadily increasing algal growth and a progressive reduction of clarity. Secchi depth has declined approximately 10 m in the last 30 years [*Jassby et al.*, 1999].

[3] Typically, thermal stratification commences around March and reaches a maximum in August, at which time the top of the thermocline is approximately 20 m below the water surface. Slow weakening of the stratification may lead to approximately isothermal conditions by February in about one year in four [*Jassby et al.*, 1999]. Several investigators have noted evidence of internal waves in Lake Tahoe, although the internal wave climate is largely undocumented [*Thompson*, 2000].

[4] The energy imparted by the wind to a stratified lake leads to basin-scale internal waves. These waves provide a driving force for vertical and horizontal transport in stratified lakes [*Imberger*, 1998; *MacIntyre et al.*, 1999], and need to be accurately modeled for the correct simulation of the dynamics of nutrients and particles. The spatial characteristics and oscillation periods of individual internal wave modes are controlled by the density stratification, the geometric properties of the enclosing basin, and, in the case of large lakes, by the Earth's rotation [e.g., *Imboden*, 1990]. The internal oscillations are either Kelvin or Poincaré waves. Kelvin waves are long gravity waves with subinertial frequencies that are trapped at the boundaries of the lake. The perturbations travel cyclonically (counterclockwise) around a basin in the Northern Hemisphere with amplitudes exhibiting an exponential decay offshore with a scale of O(Λ), the internal Rossby radius of deformation. The velocity fields show maxima at the boundaries (where the motion is rectilinear), and the current vectors in the lake interior rotate cyclonically [see, e.g., *Hutter*, 1984; *Antenucci and Imberger*, 2001]. Poincaré modes are also progressive waves. In the Poincaré modes (or rotating internal seiches) the perturbations propagate anticyclonically with superinertial frequencies. As shown by *Antenucci et al.*

Copyright 2003 by the American Geophysical Union.
0148-0227/03/2001JC000942

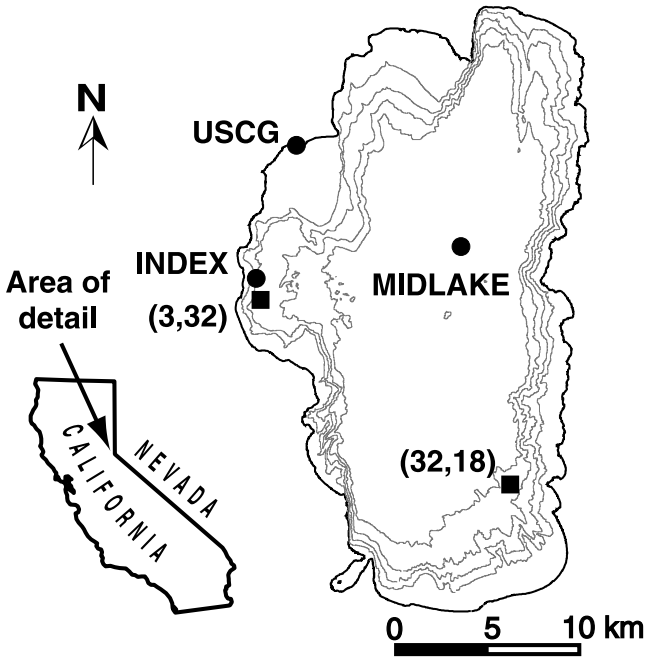

Figure 1. Lake Tahoe bathymetry (contoured on 100 m intervals) and instrument locations (circles). Thermistor chain locations are MIDLAKE and INDEX. USCG indicates the location of the meteorological station. Locations used in the analysis of the model output (squares) are identified by the column and row numbers that they occupy in the computational grid.

[2000], the isopycnal displacements induced by a Poincaré wave measured in cross section have a standing structure and are, in general, undistinguishable from those induced by a linear seiche. Poincaré waves, however, differ from the linear seiches in that the velocity vectors rotate anticyclonically. The maximum amplitudes of the water velocity induced by the wave are observed at the center of the basin. Thus the origin of isopycnal oscillations (either a linear seiche or a Poincaré wave) can only be positively confirmed by inspection of the velocity vectors at a single location or inspection of temperature records from multiple locations.

[5] Early studies on internal oscillations used simplified analytical formulations in which lakes were represented as simple domains having two-layer density stratification. With increased computer power more sophisticated numerical models were developed that allowed for arbitrary bathymetry [*Horn et al.*, 1986], continuous stratification [*Monismith*, 1987], or both of these combined [*Munnich*, 1996; *Fricker and Nepf*, 2000]. In all cases, rotational effects were neglected. *Munnich* [1996] and *Fricker and Nepf* [2000], for example, assumed that the internal waves can be represented using a 2-D vertical model aligned with the principal axis of the lake, an approach that may be justified for narrow lakes. The first analytical formulation that accounted for Coriolis effects considered circular flat bottom domains with a two-layer stratification [*Csanady*, 1973]. *Schwab* [1977] also incorporated rotational effects in the analysis of internal oscillations in two-layer systems of arbitrary planform but assumed a uniform equivalent depth. In all these cases the internal waves are analyzed using eigenvalue techniques, which precludes the combination of arbitrary geometry, continuous stratification, rotational effects, and a temporally and spatially variable wind field with the internal wave climate of the basin. By contrast, the combination of these factors and their influence on the basin-scale internal waves can be realistically represented in a 3-D hydrodynamic model.

[6] In this study the basin-scale internal wave climate of Lake Tahoe during winter cooling is characterized by using a three dimensional (3-D) hydrodynamic model [*Smith*, 1997; *Rueda and Schladow*, 2002]. The 3-D model results are combined with a theoretical analysis of the initial conditions, using simplified models of the lake geometry, and the statistical analysis of the observations from two thermistor chains and a current meter. While the simulation of basin-scale internal waves with 3-D models has been the subject of recent work by *Hodges et al.* [2000] and *Antenucci et al.* [2000] in Lake Kinneret, *Saggio and Imberger* [1998] in Lake Biwa, and *Beletsky and O'Connor* [1997] in the Great Lakes, the present study is distinctive in several important respects. First, the stratification in Lake Tahoe is extremely weak and spread over a broad metalimnion. Such conditions pose challenges to models, as numerical diffusion and phase errors can dominate and obscure the underlying physical processes. Thus, as a test of a 3-D modeling approach, the present case is severe. Second, the length scales at Lake Tahoe define a different set of conditions. While the horizontal scales are the same order of magnitude as those in Lake Biwa and Lake Kinneret, the vertical scale is an order of magnitude larger in Lake Tahoe. This depth, combined with the weak stratification, results in vertical excursions of the internal waves frequently exceeding 50 m at the lake margins (Figure 2c), producing enhanced horizontal gradients near the boundaries. Lake Tahoe and the Great Lakes differ in horizontal scale by an order of magnitude, resulting in Rossby numbers of $O(10^{-1})$ and $O(10^{-2})$ respectively. As the characteristics of the flow field vary greatly with the values of the Rossby number [*Cushman-Roisin*, 1994] it is expected that the two cases will be fundamentally different. Third, at Lake Kinneret the internal wave climate was driven by a highly regular, diurnal, summer sea breeze. The present study was performed during winter when series of energetic storms act on the lake. The associated wind during these storms has the most dramatic influence on the internal wave climate of Lake Tahoe. The timing of the storms does not follow a clear pattern, and the wind field associated with each of the storms does not have a clear directional character. As will be shown, the phase between the periodic internal wave field and the aperiodic storm wind field is a critical feature that accounts for much of the evolution of the internal dynamics of Lake Tahoe, and probably in many other lakes.

2. Methods

2.1. Field Observations

[7] Two thermistor chains were deployed in Lake Tahoe during winter 1999–2000 to provide continuous record of the winter temperature and density structure (Figure 1). One of the chains was deployed at the INDEX station, a site near the west shore (N 39°6.744′, W 120°8.932′) with a depth of

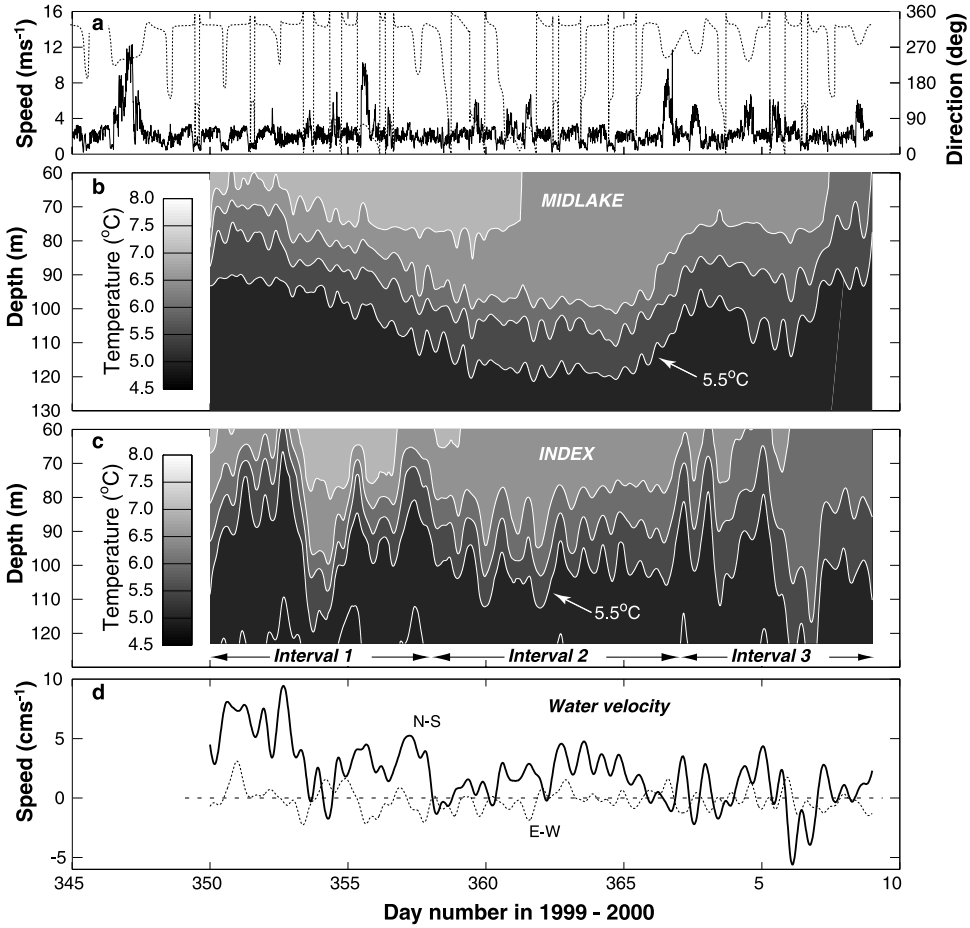

Figure 2. Time series of (a) wind speed and direction, (b) isotherm depths at the MIDLAKE station, (c) isotherm depths at the INDEX station, and (d) horizontal velocity components measured 7 m below the free surface at the INDEX station. All variables are presented with a 6-hour moving average filter, except for the wind speed, which shows 10 min averages. Isotherms in Figures 2b and 2c are shown every 0.5°C. Here 5.5°C has been marked for reference. The period under analysis started on day 350 1999 (16 December) and ended on day 9 2000 (9 January).

approximately 124 m. The second thermistor chain was deployed closer to the center of the lake, at the MIDLAKE station (N 39°7.535′, W 120°0.731′), where the depth is approximately 464 m. The time series of temperature analyzed in this work are 24-day segments from the larger data set collected during the winter months of 1999–2000. The time series start on day 350 1999 (16 December) and end on day 9 2000 (9 January). Water temperature was sampled at 2-min intervals, using Oregon Environmental Instruments 9311, Richard Brancker Research TR-1000F and Seabird SBE-39 thermistors. The thermistors were calibrated to an accuracy of better than 0.005°C and attached at 10 to 40 m intervals, with the closer spacing near the surface. A Sontek Argonaut velocity meter was placed on the INDEX mooring chain at 7 m below the free surface. It measured velocity in a single 1 m vertically integrated bin at 20 min averaged intervals. Meteorological data were collected at the dock of the Tahoe U.S. Coast Guard station (N 39°10.838, W120°07.157′). Figure 2a displays the time series of wind data. In addition, shortwave radiation, air temperature and relative humidity data were recorded at 10-min intervals during this period. Details on the thermistor chains and the weather station are described by *Thompson* [2000].

[8] The internal wave field was analyzed using power spectra and wavelet transforms of the integrated potential energy (IPE) and integrated kinetic energy (IKE), defined as

$$IPE(t) = \int_{z_0}^{z_1} \rho(z,\ t)\ g\ z\ dz \tag{1a}$$

$$IKE(t) = \frac{1}{2} \int_{z_0}^{z_1} \rho(z,\ t)\ \left(u^2 + v^2\right) dz \tag{1b}$$

The IPE gives a clear and concise picture of the frequency content of the internal wave field and also of the relative distribution of potential energy among frequencies [*Antenucci et al.*, 2000]. IKE accomplishes the same for the horizontal kinetic energy [see *Antenucci and Imberger*, 2001]. Here, z is the vertical coordinate, g is the acceleration of gravity, ρ is density, u and v are velocities in the two

horizontal components, and z_0 and z_1 represent the bottom and top of the water column respectively. Spectral estimates in the Fourier analysis were averaged in the frequency domain to improve confidence [*Saggio and Imberger*, 1998]. Continuous wavelet transform was used for time-frequency analysis, adopting the Morlet wavelet [*Torrence and Compo*, 1997]

$$\psi(t) = \pi^{-1/4} \exp\left(-\frac{t^2}{2}\right) \exp(i\omega_0 t), \tag{2}$$

with $\omega_0 = 6$ as mother wavelet. The continuous wavelet transform of the IPE time series is defined as

$$C(s,t) = \int_{-\infty}^{+\infty} IPE(u)\psi_{s,t}(u)du \tag{3}$$

where

$$\psi_{s,t}(t) = \frac{1}{\sqrt{s}}\psi(t)\left(\frac{u-t}{s}\right) \tag{4}$$

The coefficient C represents the characteristics of the IPE signal at scale s. The scale s in the Morlet wavelet utilized here and the equivalent Fourier period T are approximately equal, with $T = 1.03\ s$ [*Torrence and Compo*, 1997]. Identical expressions pertain to the continuous wavelet transform of the IKE time series.

[9] All averaging refers to time averages of temperature records obtained by individual thermistors. Although *Thorpe et al.* [1996] suggest that averaging should be performed on the depth of the isotherms, to reduce uncertainty, this was not considered warranted. It was considered that far greater uncertainties reside in the model initial conditions and model inputs (such as the areal wind field) than in the choice of a method for time-averaging of temperature profiles.

2.2. Three-Dimensional Model for Flow and Transport

2.2.1. Governing Equations and Boundary Conditions

[10] A 3-D free surface hydrodynamic model was used to simulate the evolution of the internal wave field. The model is based on the continuity equation for incompressible fluids, the Reynolds-averaged form of the Navier-Stokes equations for momentum, the transport equation for temperature, and an equation of state relating temperature to fluid density. The governing equations, incorporating the hydrostatic and Boussinesq approximations, may be written in Cartesian rectangular coordinates as

$$\frac{\partial u}{\partial x} + \frac{\partial v}{\partial y} + \frac{\partial w}{\partial z} = 0 \tag{5}$$

$$\frac{\partial u}{\partial t} + u\frac{\partial u}{\partial x} + v\frac{\partial u}{\partial y} + w\frac{\partial u}{\partial z} - fv = -g\frac{\partial \zeta}{\partial x} + \frac{g}{\rho_0}\int_z^{\zeta} \frac{\partial \rho}{\partial x}dz' + \frac{\partial}{\partial x}\left(K_H\frac{\partial u}{\partial x}\right) + \frac{\partial}{\partial y}\left(K_H\frac{\partial u}{\partial y}\right) + \frac{\partial}{\partial z}\left(K_V\frac{\partial u}{\partial z}\right) \tag{6}$$

$$\frac{\partial v}{\partial t} + u\frac{\partial v}{\partial x} + v\frac{\partial v}{\partial y} + w\frac{\partial v}{\partial z} + fu = -g\frac{\partial \zeta}{\partial y} + \frac{g}{\rho_0}\int_z^{\zeta} \frac{\partial \rho}{\partial y}dz' + \frac{\partial}{\partial x}\left(K_H\frac{\partial v}{\partial x}\right) + \frac{\partial}{\partial y}\left(K_H\frac{\partial v}{\partial y}\right) + \frac{\partial}{\partial z}\left(K_V\frac{\partial v}{\partial z}\right) \tag{7}$$

$$\frac{\partial T}{\partial t} + u\frac{\partial T}{\partial x} + v\frac{\partial T}{\partial y} + w\frac{\partial T}{\partial z} = \frac{\partial}{\partial x}\left(D_H\frac{\partial T}{\partial x}\right) + \frac{\partial}{\partial y}\left(D_H\frac{\partial T}{\partial y}\right) + \frac{\partial}{\partial z}\left(D_V\frac{\partial T}{\partial z}\right) + \frac{1}{\rho c_p}\frac{\partial I}{\partial z} \tag{8}$$

$$\rho = \rho(T) \tag{9}$$

[11] Due to the Boussinesq approximation the density is neglected everywhere except in the buoyancy term. In the hydrostatic approximation, it is assumed that the weight of the fluid identically balances the pressure in the conservation equation for vertical momentum. The nonhydrostatic terms can be safely neglected as long as the internal waves being represented have much longer horizontal wavelengths than their vertical wavelengths, which is the case for basin-scale oscillations (Appendix A). Another limitation of the hydrostatic model relates to the fact that frequency dispersion is not represented [e.g., *Bauer et al.*, 1994], but simple scaling arguments based on the observations suggest that these effects can also be safely neglected in the simulations of basin-scale waves in Lake Tahoe. In equations 5 through 9, the velocity components in the x, y, and z directions are denoted by u, v, and w, f is the Coriolis parameter, g is the acceleration of gravity, ρ is water density variation with respect to a mean reference value ρ_0, T is the temperature and ζ is the water surface elevation above an undisturbed level at $z = 0$. The coefficients K_H and K_V represent the horizontal and vertical turbulent momentum transfer coefficients (or kinematic eddy viscosity), and D_H and D_V are the horizontal and vertical turbulent transfer coefficients (eddy diffusivity) for temperature. The last term in equation 8 is a source-sink term representing the divergence of the downward solar irradiance I, where c_p is the heat capacity of water. The attenuation of the solar irradiance I with depth z from its value at the free surface I_0 is modeled in terms of two length scales, L_1 and L_2, and an empirical constant, R, using a law of the form [*Rosati and Miyakoda*, 1988]

$$I = I_0\left[R\ \exp\left(-\frac{z}{L_1}\right) + (1-R)\ \exp\left(-\frac{z}{L_2}\right)\right] \tag{10}$$

[12] An equation for ζ is obtained by integrating the continuity equation (equation 5) over the water column and combining it with the kinematic boundary condition at the free surface,

$$\frac{\partial \zeta}{\partial t} + \frac{\partial}{\partial x}\left[\int_{-H}^{\zeta} udz\right] + \frac{\partial}{\partial y}\left[\int_{-H}^{\zeta} vdz\right] = 0 \tag{11}$$

Here $z = -H$ (x, y) is the depth of the bottom boundary measured from the undisturbed free surface $z = 0$.

[13] The boundary conditions at the free surface, $z = \zeta\ (x, y, t)$, are

$$\rho_0 K_V \left(\frac{\partial u}{\partial z}, \frac{\partial v}{\partial z}\right) = \left(\tau_{0x},\ \tau_{0y}\right); \rho_0 D_V \left(\frac{\partial T}{\partial z}\right) = H_S \qquad (12)$$

where (τ_{0x}, τ_{0y}) is the surface wind stress vector, and H_S represents the net effect of the nonpenetrative components of the heat flux (evaporation, conduction and long-wave radiation). The fluxes of heat (H_S) and momentum (τ_{0x}, τ_{0y}) at the free surface are calculated using a bulk parameterization [*Kondo*, 1975; *Liu and Schwab*, 1987]. At the lower boundary, $z = -H\ (x, y)$,

$$\rho_0 A_V \left(\frac{\partial u}{\partial z}, \frac{\partial v}{\partial z}\right) = \left(\tau_{\mathrm{bx}},\ \tau_{\mathrm{by}}\right); w|_{z=-H} = -u\frac{\partial H}{\partial x} - v\frac{\partial H}{\partial y}; \left(\frac{\partial T}{\partial n}\right) = 0 \qquad (13)$$

Here, n is the direction normal to the bottom boundary and $(\tau_{\mathrm{bx}}, \tau_{\mathrm{by}})$ is the bottom frictional stress which is determined from the bottom velocity (u_b, v_b) by a quadratic law of the form

$$\left[\tau_{\mathrm{bx}},\ \tau_{\mathrm{by}}\right] = C_d \sqrt{u_b^2 + v_b^2}[u_b,\ v_b] \qquad (14)$$

where C_d is a drag coefficient, considered constant in the model. Along the shoreline, in the horizontal direction, a perfect slip condition is imposed in which the water is allowed to move parallel to the shoreline without any resistance. No heat flux is permitted across lateral or bottom boundaries, which given the depth of Lake Tahoe, is a safe assumption. The possible effects on the bottom boundary layer of near bed-stratification caused by sediment or chemical concentration [*Dimai et al.*, 1994] are neglected, given the limited information that exists on Lake Tahoe. Stratification in the model arises purely by temperature differences.

2.2.2. Numerical Solution of the Hydrodynamic and Transport Equations

[14] The grid system is composed of horizontal layers, and the governing equations are integrated over the height of each layer. The model uses a semi-implicit three-level leapfrog-trapezoidal finite difference scheme on a staggered Cartesian grid (Arakawa C grid) to solve the layer-averaged form of the 3-D shallow water and transport equations [*Smith*, 1997]. The semi-implicit approach for the hydrodynamic equations is based on treating the gravity wave and vertical diffusion terms implicitly to avoid time step limitations due to gravity-wave CFL conditions, and to guarantee stability of the method. All other terms, including advection, are treated explicitly. The leapfrog-trapezoidal algorithm used for time stepping gives second order accuracy both in time and space.

2.2.3. Dissipation and Phase Lag in the Numerical Algorithm

[15] The ability of the numerical model to simulate internal oscillations was verified against the analytical solution for internal seiches in a rectangular basin with flat bottom and uniform stratification, given by *Eliason and Bourgeois* [1997]. The analytical solution assumes that (1) the motion is effectively 2-D in a vertical plane, (2) the fluid is inviscid and (3) nonlinear terms can be neglected. The code was modified accordingly to solve the governing equations assumed in the analytical solution, and it was set up to simulate the first vertical and horizontal internal seiche in a 20000 × 4000 × 12 m basin, with constant buoyancy frequency $N = 0.04045\ \mathrm{s}^{-1}$, and velocity amplitude of 10 cm s^{-1}. A time step $\Delta t = 720$ s, and 2000 × 2000 × 1 m cells were used to discretize the problem. At the end of the 6 day simulation period the stratification had not changed significantly in the basin. Analytical and numerical solutions are compared in Figure 3. The amplification factor and the celerity ratio of the numerical scheme [e.g., *Gray and Lynch*, 1979], calculated by comparing the surface velocity from the two solutions in the center of the basin, were 1.0000 and 1.0019 respectively (1.069 for the density at the end of the basin). These values indicate that the solution scheme is essentially free of numerical dissipation, and for the grid used it displayed only a slight phase shift. Assuming that the accuracy of the internal wave representation is similar in Lake Tahoe as that in the numerical experiment, the estimated lag in 18-hour period waves is approximately 2 min. A principal determinant of the phase shift is the ratio of wavelength to grid size, $\lambda/\Delta x$, with larger values reducing the phase shift. For the test case this ratio had a value of 20. For the first horizontal mode lateral seiche in Lake Tahoe, and the 500 m grid used, $\lambda/\Delta x \sim 80$, and hence we would expect less phase shift in its numerical simulation.

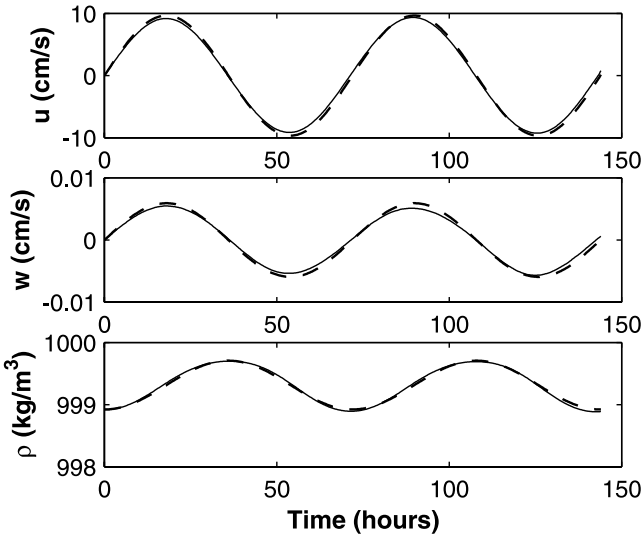

Figure 3. Verification exercise: time series of simulated (solid line) and analytical (dashed line) results for horizontal velocity, vertical velocity, and density in a rectangular basin.

2.2.4. Turbulence Model

[16] The 3-D lake model uses a modified formulation of the 2.5 level Mellor-Yamada turbulence closure scheme to parameterize vertical mixing [*Kantha and Clayson*, 1994]. This formulation incorporates the quasi-equilibrium turbulence model (QETE) of *Galperin et al.* [1988] with readjusted parameters, and a parameterization of shear-instability-induced mixing in the strongly stratified region below the surface mixed layer. It was developed to correct some of the deficiencies of the original formulation of the Mellor-

Yamada 2.5-Level closure scheme, which was shown to misrepresent the depth of the surface mixed layer in oceanic applications [e.g., *Martin*, 1985]. Two partial differential equations are used to calculate the turbulent kinetic energy, $q^2/2$, and a turbulent macroscale, l, given by

$$\frac{\partial q^2}{\partial t} - \frac{\partial}{\partial z}\left(lqS_q\frac{\partial q^2}{\partial z}\right) = 2[P_s + P_b - \varepsilon] \tag{15}$$

$$\frac{\partial(q^2 l)}{\partial t} - \frac{\partial}{\partial z}\left(lqS_q\frac{\partial(q^2 l)}{\partial z}\right) = lE_1[P_s + P_b] - \frac{q^3}{B_1} \cdot \left[1 + E_2\left(\frac{l}{\kappa z}\right)^2 + E_3\left(\frac{l}{\kappa(H-z)}\right)^2\right] \tag{16}$$

Here, κ is the von Karman constant, and P_s, P_b and ε stand for shear production, buoyant production and the dissipation of turbulent kinetic energy, given by

$$P_s = K_v\left(\frac{\partial u}{\partial z}\right)^2 + K_v\left(\frac{\partial v}{\partial z}\right)^2; \quad P_b = \frac{g}{\rho_0}D_v\frac{\partial \rho}{\partial z}; \quad \varepsilon = \frac{q^3}{B_1 l} \tag{17}$$

in which B_1 is an empirical constant. The boundary conditions applied at the top and the bottom boundaries are calculated from the friction velocity u^* as [*Blumberg*, 1986]

$$q^2 = B_1^{2/3}(u_*)^2, \qquad q^2 l = 0 \tag{18}$$

[17] The turbulent fluxes of momentum (u, v) and temperature (T) are represented using a diffusion model and the concepts of eddy viscosity and diffusivity. The eddy viscosity and diffusivity are calculated from q and l as $K_V = S_m lq$ and $D_V = S_h lq$ in which S_m and S_h are stability functions that account for the effects of stratification on mixing. They are calculated as [*Kantha and Clayson*, 1994]

$$S_h = \frac{A_2\left(1 - \frac{6A_1}{B_1}\right)}{1 - 3A_2G_h(6A_1 + B_2(1 - C_3))} \tag{19}$$

$$S_m = A_1\frac{\left(1 - \frac{6A_1}{B_1} - 3C_1\right) + 9[2A_1 + A_2(1 - C_2)]S_hG_h}{(1 - 9A_1A_2G_h)} \tag{20}$$

$$G_h = -\left(\frac{Nl}{q}\right)^2 \tag{21}$$

The values of the constants in the model are (A_1, A_2, B_1, B_2, C_1, C_2, C_3, S_q, E_1, E_2) =(0.92, 0.74, 16.6, 10.1, 0.08, 0.7, 0.2, 0.2, 1.8, 1.33) as suggested by *Kantha and Clayson* [1994]. G_h is bounded from above, so that the variance of the velocity fluctuations are positive definite, according to

$$G_h \le \{A_2[B_1 + 12A_1 + 3B_2(1 - C_3)]\}^{-1} \tag{22}$$

The upper bound on G_h is set to 0.029 [*Kantha and Clayson*, 1994]. The lower bound on G_h reflects that under strong stable stratification conditions, there is a limit to the size beyond which eddies are incapable of overturning. This bound is dictated by the Ozmidov scale, $L_o = (\varepsilon/N^3)^{1/2}$, and is given by $G_h > -0.28$.

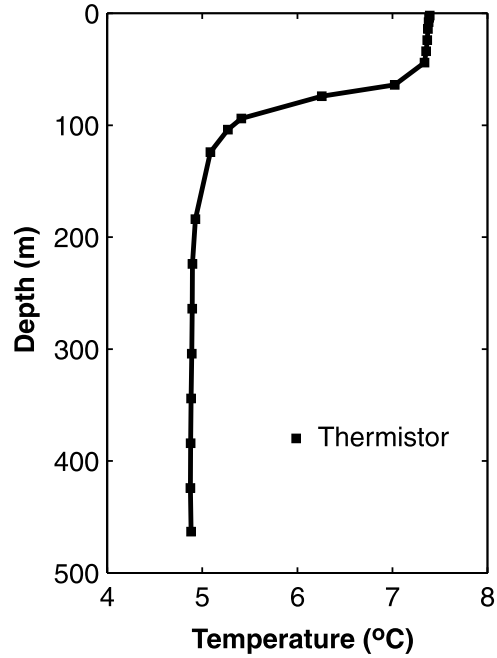

Figure 4. Vertical temperature distribution obtained by time-averaging temperature records at the MIDLAKE station from day 350 to day 354 1999. The locations of the thermistors are indicated by squares.

[18] A 3-level, fully implicit algorithm is adopted for the numerical solution of the turbulence equations [*Fletcher*, 1991]. The method has a truncation error of $O(\Delta t^2, \Delta x^2)$, is A-stable and damps out spurious oscillations associated with stiff problems. The numerical algorithm is presented in Appendix B. The mixing routines were tested against other deepening laws and mixed-layer models published in the literature [*Kato and Phillips*, 1969; *Pollard et al.*, 1973; *Kundu*, 1980; *Sherman et al.*, 1978] giving very satisfactory results [see *Rueda*, 2001].

3. Measured Response in Lake Tahoe

3.1. Evolution of the Internal Wave Climate

[19] Figure 2 displays the evolution of isotherm depths, at the MIDLAKE and INDEX stations, obtained from 6-hour moving averages of the temperature record. No indication exists in those observations of vertical oscillation modes higher than 1, hence only first vertical modes will be considered in the discussion that follows. The time series of the 5.5°C isotherm (obtained by vertical linear interpolation from individual temperature records) will be used as a reference. This isotherm is located close to the base of the metalimnion (Figure 4), and it will hence experience significant oscillations due to internal waves.

[20] Observations at the INDEX station suggest that three intervals of internal wave activity can be distinguished (Figure 2): (1) interval 1 (days 350 through 357 in 1999) with significant internal wave activity at both subinertial and superinertial frequencies, and amplitudes of up to 30 m; (2) interval 2 (from day 358 1999 through day 1 2000) where the subinertial oscillations observed in Interval 1 with

periods above 24 hours vanish; the diurnal and superinertial periodicity dominate during this interval; (3) interval 3 (from day 2 2000 to the end of the record) when the wind again excites the internal waves at the periods previously observed during Interval 1.

[21] At the MIDLAKE station these intervals are not present. Instead, over the first 15 days the isotherms initially deepen (the 5.5°C isotherm descends from 90 m to 120 m) and the surface layer cools. Internal oscillations with lower than diurnal periodicity are observed throughout this time. Then, starting approximately day 365 1999, the isotherms rise, with the 5.5°C isotherm, for example, rising from 120 m to approximately 90 m. The upward migration of the isotherms seems to suggest that processes of larger timescales than those of the internal waves exist in the lake. Those are most probably driven by seasonal differential cooling and lateral advection, as suggested by *Thompson* [2000]. Satellite imagery (not shown) for the first days of 2000 confirmed significant surface temperature spatial variation between shallow boundary areas and the center of the lake, with the former being much colder (S. J. Hook, unpublished data, 2000). The picture, here outlined, of the evolution of the internal wave field in both observation stations is supported by the wavelet analysis (not shown) applied to the IPE time series.

3.2. General Features of the Water Column

[22] The speed of propagation of first vertical mode internal waves c was estimated on a daily basis by solving the eigenvalue problem for the spatial structure of internal waves in nonrotating frames [*Kundu*, 1990], using the temperature records from the MIDLAKE station. The background stratification was determined for each daily window by averaging temperature records for each of the thermistors on the chain. Initially (first 15 days), the speed of propagation is approximately constant at about 0.240 ± 0.004 m s^{-1}, reducing to approximately 0.18 m s^{-1} on the last day of the experiment. Based on a mean temperature profile obtained by time-averaging the temperature records at the MIDLAKE station for the first three days of the 24-day period (Figure 4) the estimated speed of propagation is 0.240 m s^{-1}. The internal Rossby radius of deformation, defined as

$$\Lambda = \frac{c}{f} \tag{23}$$

is about 3 km for the first vertical mode internal waves, well below the width of Lake Tahoe (~20 km), suggesting that internal oscillations are either Kelvin or Poincaré modes.

[23] Using daily averaged temperature profiles at MIDLAKE, one can estimate, on the basis of timescales and dimensionless numbers, the expected response of the water column. For example, the steepening timescale [*Horn et al.*, 2001] for Lake Tahoe was estimated to be approximately 50–100 days, which is much longer than the timescale of the Kelvin waves in Lake Tahoe as observed in the short observation period of this experiment. Hence nonlinear steepening, and probably wave dispersion effects, can be initially neglected in the study of the basin-scale internal waves in Lake Tahoe. The Lake (L_N) and Wedderburn (W) numbers, which parameterize the response of the water column to a constant wind stress [*Imberger and Patterson*, 1990], are well above unity throughout this period, suggesting relatively small isotherm displacements compared to the thickness of the surface layer and little possibility of imminent lake overturn.

Table 1. Comparison of Periods Found in the Numerical Simulations With Those Found in the Observations and Predicted by the Analytical Circular Model[a]

Oscillatory Mode	IPE Observations	Velocity Observations	IPE Simulations	Velocity Simulations	Analytical Model
KW H1V1	127.6	124.3	133.4	135	113[b]
KW H2V1	56.8	57.9	60.3	62.1	57[b]
KW H3V1	–	36.2	–	39.3	37.6[b]
Diurnal	23.7	25.9	29.6	25.2	–
PW H1V1	17.6	16.9	16.6	16.9	16.1–17.8

[a]Periods are in hours.
[b]Based on a 34,000 m diameter circular model.

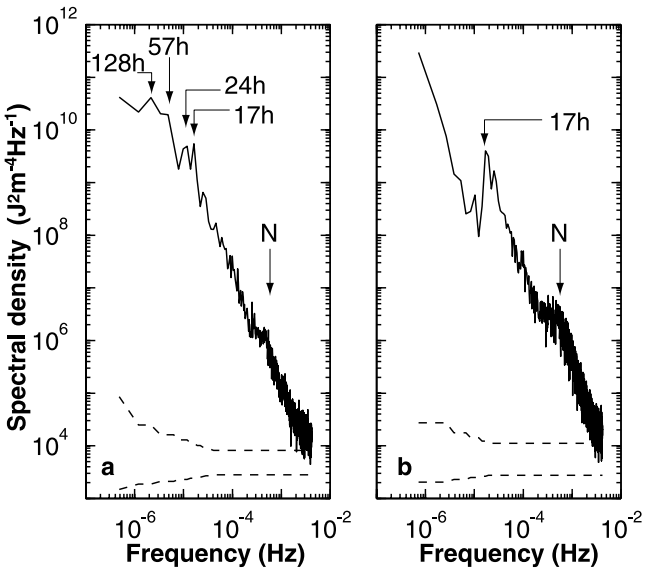

Figure 5. Power spectra of integrated potential energy (IPE) at (a) INDEX and (b) MIDLAKE stations. Dashed lines indicate 95% confidence levels.

3.3. Spectra of Integrated Potential Energy

[24] The power spectra of IPE from the INDEX and MIDLAKE stations are shown in Figures 5a and 5b. The spectrum at MIDLAKE reveals energetic oscillations at $\omega \sim 1.6\ 10^{-5}$ Hz (17 h period), a decay of the energy with ω^{-2}, as in the Garret-Munk internal wave model [*Garret and Munk*, 1979], and an accumulation of energy again at the buoyancy frequency of the thermocline ($N \sim 6 \times 10^{-4}$ Hz). Very little energy exists at frequencies below the inertial frequency ($\omega \sim 9 \times 10^{-4}$ Hz). At the INDEX station, the IPE spectrum shows peaks at approximately 128, 58, 24, and 17 hours (Table 1), and, as was the case at MIDLAKE, a characteristic ω^{-2} energy decay and a slight increase of energy at the buoyancy frequency. The superinertial frequency (corresponding to the 17 h period) represents the characteristic signature of a Poincaré wave, which can be detected throughout the lake. Due to its nearshore location, the chain at the INDEX station also detects the presence of

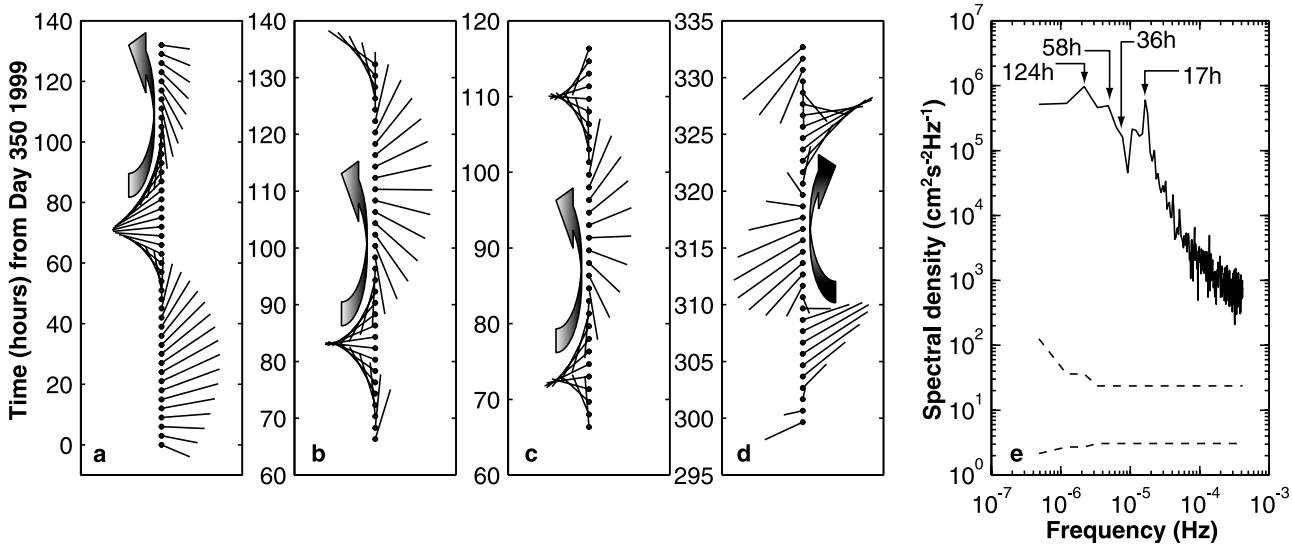

Figure 6. Vector plots of band-pass filtered velocity records for segments of the data set that reveal the sign of rotation: (a) H1V1 Kelvin wave with period of 128 h, (b) H2V1 Kelvin wave with period of 55 h, (c) H3V1 Kelvin wave with period of 37 h, and (d) H1V1 Poincaré wave with period of 17 h. (e) Total spectrum of the velocity records showing peaks with those periods encountered in the analysis of isotherm displacements.

subinertial Kelvin waves. The peaks at $\omega \sim 10^{-5}$ Hz (a period of 24 h) in the spectra at both the INDEX and MIDLAKE stations correspond to the weak diurnal periodicity of the wind-forcing. These same features are revealed by the wavelet transform.

3.4. Spectra of Velocity

[25] The total spectrum of the velocity records measured by the surface meter at the INDEX station (Figure 6e) also reveals peaks at the same frequencies observed in the spectra of IPE time series. It shows, furthermore, a concentration of energy at approximately 7.7×10^{-6} Hz (36 h period). All peaks, but that with diurnal periodicity, most likely represent the signature of free-internal oscillations. The rotational behavior of the vector time series at each of those characteristic frequencies was exposed by first isolating the oscillations with a Butterworth digital band-pass filter (see Table 2) and then displaying the filtered velocity components as vector plots (Figures 6a–6d). This reveals a velocity vector rotating cyclonically with approximately 124, 58 and 36-hour periods (Figures 6a, 6b, and 6c), consistent with the interpretation that the subinertial oscillations represent Kelvin waves. The 17-hour period vector time series shows an anticyclonic rotation (Figure 6d), characteristic of the velocity field in a Poincaré wave.

4. Analytical Model of Lake Tahoe

[26] To yield analytical estimates of the internal wave field, Lake Tahoe is approximated as a circular, flat-bottom basin with a diameter of 19,600 m (the maximum width of the basin in the east-west direction) or 34,000 m (the maximum length in the north–south direction). By changing the diameter, some uncertainty is introduced since complex bathymetry cannot be represented with such a model. The smaller diameter better represents the lake's surface area (496 km^2), while the larger diameter gives a better representation of Lake Tahoe's perimeter (108 km). A two-layer stratification is assumed with a speed of propagation of interfacial waves, $c = 0.240$ m s^{-1}. Due to the lake's latitude ($\theta \sim 39°$), the inertial period of oscillation is 19.07 hours (inertial frequency $\sim 9.189\ 10^{-5}$ s^{-1}). The solution to the inviscid linear equations of motion in a circular flat bottom basin with a two-layer stratification is given by *Csanady* [1967] and it has recently been reviewed by *Antenucci et al.* [2000]. Two kinds of solutions are possible, one with subinertial frequencies (Kelvin waves) and another with superinertial frequencies (Poincaré waves).

4.1. Kelvin Waves

[27] For each azimuthal wave number n (= 1, 2, . . .) there is one Kelvin mode provided that the condition [*Csanady*, 1967]

$$\beta = \frac{f^2 R_0^2}{c^2} > n(n+1) \tag{24}$$

is met. For Lake Tahoe, β will vary from 12 to 40, depending on the dimensions of the circular model, and the basin can support Kelvin waves with up to 3–5 nodal diameters. Based on the analytical model presented by *Csanady* [1967] and using values for the largest circular

Table 2. Parameters in the Design of Butterworth Filters Used to Isolate the Internal Wave Oscillations

Oscillatory Mode	Filter Order	Passband, Hz ω_{min}	Passband, Hz ω_{max}
KW H1V1	5	2.069×10^{-6}	2.986×10^{-6}
KW H2V1	4	4.250×10^{-6}	7.528×10^{-6}
KW H3V1	3	6.333×10^{-6}	9.083×10^{-6}
PW H1V1	3	1.600×10^{-5}	1.733×10^{-5}

model of Lake Tahoe, the following characteristic periods can be estimated: 113 ± 2 hours for the first azimuthal mode (one nodal diameter), 57 ± 1 hours for the second mode (two nodal diameters), and 38 ± 1 hours for the third azimuthal mode (three nodal diameters). For the fourth and fifth azimuthal modes the periods are estimated to be approximately 28 and 22 hours respectively. These latter two periods are not observed in any of the experimental records and hence they are not considered further. The larger circular model was used, since it approximates better the perimeter of Lake Tahoe. These estimates agree with those given by dividing integer multiples of the perimeter P by the speed of propagation of the internal wave in the absence of rotation [*Csanady*, 1973; *Hodges et al.*, 2000].

4.2. Poincaré Waves

[28] In this case, for fixed n, the individual solutions to the inviscid linear equations of motion may be distinguished by the number m of nodal circles present in the corresponding pattern of surface and interface elevations. The spatial pattern of the Poincaré waves will hence consist of cells of radial dimensions $r_j - r_{j-1}$ (r_j = radius of the jth nodal circle) and of angular width $(\pi + 2k\pi)/2n$, with $k = 0, 1, 2, \ldots$ [*Csanady*, 1967]. For the circular model of Lake Tahoe, the solution of the frequency equation indicates that only the lowest modes have a frequency close to the inertial frequency. The two-layer circular models predicts Poincaré waves of the first azimuthal mode with a characteristic period ranging from 17.84 ± 0.04 hours for the larger diameter to 16.12 ± 0.08 hours for the smaller diameter.

5. The 3-D Model of Lake Tahoe

5.1. Model Setup

[29] Bathymetric information at 500 m resolution was extracted from a recent bathymetric survey of Lake Tahoe [*Gardner et al.*, 1998]. This horizontal grid spacing, about 20% of the Rossby radius, allows for an accurate representation of the Kelvin wave phase speed [*Schwab and Beletsky*, 1998]. The vertical dimension of Lake Tahoe was discretized using 5 m cells. The total number of computational cells in the grid was 325136, of which almost 80% were wet (active in the computations). The time step was set to Δt = 300 seconds and the results were saved every 1800 seconds. In each time step, two trapezoidal iterations were performed after the initial leapfrog step, which in previous tests had given very satisfactory results [*Rueda*, 2001]. The simulation started on day 346 1999, to capture the observed oscillations between days 350 and 360 1999. The simulation was initialized with a horizontally homogeneous temperature field. The initial vertical distribution of temperatures was obtained from the profile in Figure 4 by linearly interpolating to the centers of the computational cells. From day 346 to 350, heat fluxes were suppressed in the model since the initial profile approximates the background temperature distribution on day 350 (observations do not exist for day 346).

[30] To represent the attenuation of short-wave solar radiation in the water column, the values of R, L_1 and L_2 in equation 10 were set to 0.58, 0.35 m and 23 m respectively, consistent with Type I or clear water, according to the classification proposed by Jerlov (referenced by *Rosati and Miyakoda* [1988]). The simulation was driven with meteorological data collected at the U.S. Coast Guard station (Figure 1), the only station available at the time. Although this site is generally well exposed, it is likely that there are significant differences in both wind magnitude and direction across a lake of this size. Recent measurements have shown that the frequency response of the wind-forcing at this site is strongly correlated with other sites across the lake (Schladow, unpublished data). The incoming long-wave radiation was calculated using standard formulations and assuming a cloud cover fraction of 0.15, since the long-wave radiation sensor malfunctioned during the period of the simulations. The bottom drag coefficient was 0.002, as suggested for a mud bottom [*Smith*, 1997]. Given the depth of the basin, this parameter has little effect on the results. The horizontal eddy viscosity was set to a constant value of 1 m^2s^{-1}, the lowest of the range of values suggested by *Cheng et al.* [1976]. This was necessary to keep computations stable.

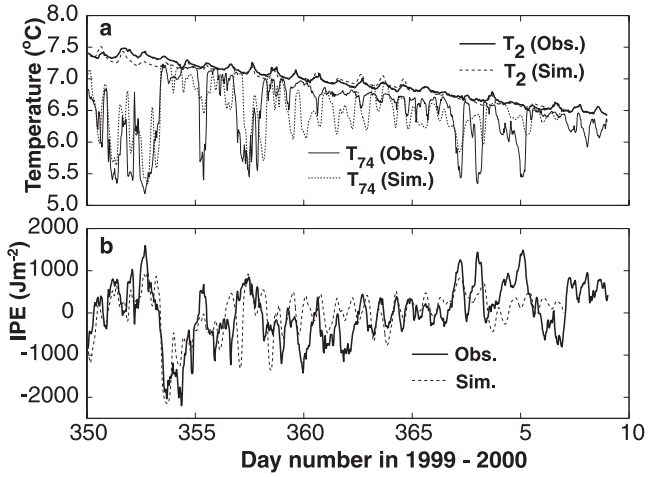

Figure 7. Comparison of observations and simulations at the INDEX station: Time series of (a) observed and simulated temperatures at 2 m and 74 m below the surface; (b) observed and simulated integrated potential energy. Station (3, 32) in the model is taken as representative of the INDEX station.

5.2. Basin-Scale Internal Waves in Model Results

[31] The model results were validated with data from the INDEX station, where the observations reveal a broad spectrum of internal waves existing in Lake Tahoe. Figure 7a compares simulated and observed temperatures at two different depths (surface and 74 m deep) at the INDEX station (station 3,32 in the model results). The thermistor at 74 m is in the upper part of the metalimnion, and experiences significant oscillations due to internal waves. Figure 7b compares simulated and observed time series of integrated potential energy at the INDEX station. This provides a global measure of the internal wave activity in the water column. The close agreement between simulated and observed surface temperatures suggests that cooling and mixing rates, that determine the surface temperature during a cooling period, are well represented in the model. The internal wave climate is not represented equally well. Even

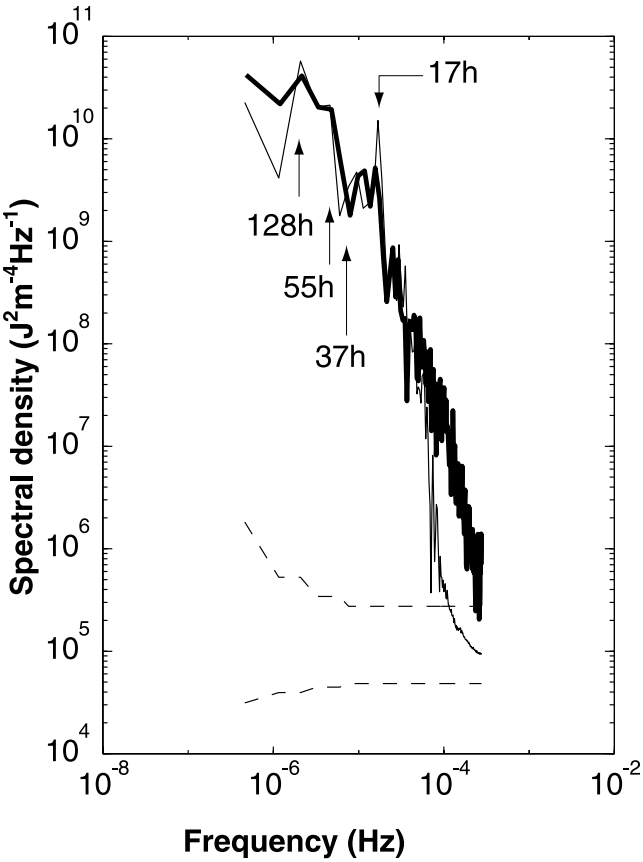

Figure 8. Spectrum of simulated (thin line) and observed (thick line) IPE at the INDEX station. Arrows mark periods identified in the analysis of observed IPE at the INDEX station. Dashed lines define confidence (95%) intervals.

though the model predicts reasonably the initial (7–10 days) period of observation, the match deteriorates as time progresses. The model captures the decay of the Kelvin waves from Interval 1 to Interval 2 of the observations, but does not reproduce the excitation of Kelvin waves in Interval 3. Possible causes of such disagreement are discussed below.

[32] Figure 8 shows the power spectrum of the simulated and observed IPE signals at the INDEX station. Both time series are sampled every 30 min for consistency. The same four peaks are encountered in the simulation and in the analysis of the thermistor chain records: three peaks in the subinertial range of the frequency, and one peak in the superinertial range. The periods found in the spectral analysis of the 3-D model results and the observations along with the periods predicted by the analytical model are compared in Table 1. The 3-D model predicts internal wave energy close to that observed, as evident by the proximity of both spectra in Figure 8, but slightly overpredicts it at the internal wave frequencies. Also, the quasi-diurnal peak in the model does not correspond exactly to the peak in the observations (closer to 24 h). The rotational character of the velocity field at each of the peaks was studied, by calculating the rotary spectra [e.g., *Fofonoff*, 1969] of the velocity records from node (32, 18, 30) in the grid (Figure 9). While the total spectrum of the velocity at node (3, 32) displays the same peaks as in the velocity observations, its rotational character is not clear, given that it is adjacent to the western boundary in the numerical grid. The choice of node (32, 18) as "observation" point is somehow arbitrary, although justified in that the rotational character of the velocity field is pronounced there (given it is far enough from the boundary), and both sub- and superinertial oscillations are detectable in the rotary spectrum (since it is within the internal Rossby radius from the boundary). The oscillations with a period of 16–18 h have a very strong anticyclonic rotating component, following the behavior expected for a Poincaré wave. The cyclonic rotating components of the velocity time series, on the other hand, dominate in the sub-inertial range of frequencies that are associated with the Kelvin modes. The spectrum shows clearly the 37 h signal. The origin of the diurnal signal seems to be associated with the weak diurnal periodicity in the wind time series, since this peak was only observed in the spectra of velocity time series close to the surface.

5.3. Spatial Structure of IPE Oscillations

[33] To visualize the spatial structure and evolution of internal wave modes in Lake Tahoe, the numerical model was set to calculate and record the IPE at every horizontal position hourly. The IPE at each horizontal location was detrended and band-pass filtered to isolate the oscillations with the characteristic frequencies revealed in the spectra. The passbands (in Hz) and order of the filters, used to isolate the different modes of oscillation, are given in Table 2. Here, results for the first 100 hours of the study period are emphasized, when the simulations most closely match the observations.

[34] Figure 10 displays the evolution of the IPE caused by the subinertial oscillations in sequences of plots at quarter-period (T/4) increments. Kelvin waves are seen traveling cyclonically around Lake Tahoe, with the shore on the right, and with one (Figures 10a, 10b, 10c, and 10d), two (Figures 10e, 10f, 10g, and 10h) and three (Figures 10i, 10j, 10k, and

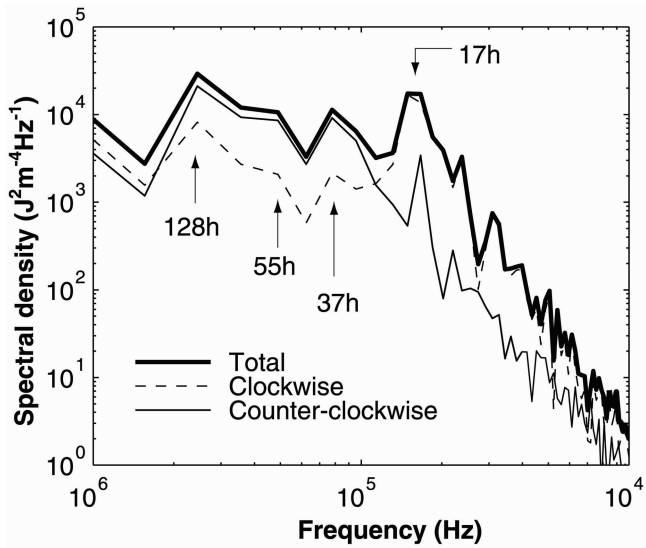

Figure 9. Rotary spectra of simulated velocity 150 m below the surface at node (32,18,30). The total spectrum is obtained by adding the anticyclonic (dashed) and cyclonic (thin solid line) components.

10l) nodal diameters. Increases in the IPE field (red) represent areas of upwelling or rising of isotherms, while troughs (blue) represent areas of downwelling or depression of the isotherms. A characteristic feature that is especially visible in the first Kelvin mode, is an away-shore "tongue" where the IPE undergoes significant oscillations. This feature trends to the south-east, out of the western embayment of Lake Tahoe. In Figure 10b it is present in a downwelled phase, while in Figure 10d it is in an upwelled phase. Careful observations of the IPE evolution show that the oscillations in this area lead those in the western embayment. The mechanism for the generation of this feature is unresolved, although it appears linked to topographical features. First horizontal mode Kelvin waves were repeatedly observed in Lake Tahoe during the four year study of *Thompson* [2000], but with periodicities that increased from 2.5–3 days in the early Fall, to values closer to those presented here, later in winter. Higher modes, though, have not previously been documented in Lake Tahoe.

[35] The spatial structure of the superinertial (17 h) oscillations of the IPE field is illustrated in the sequence

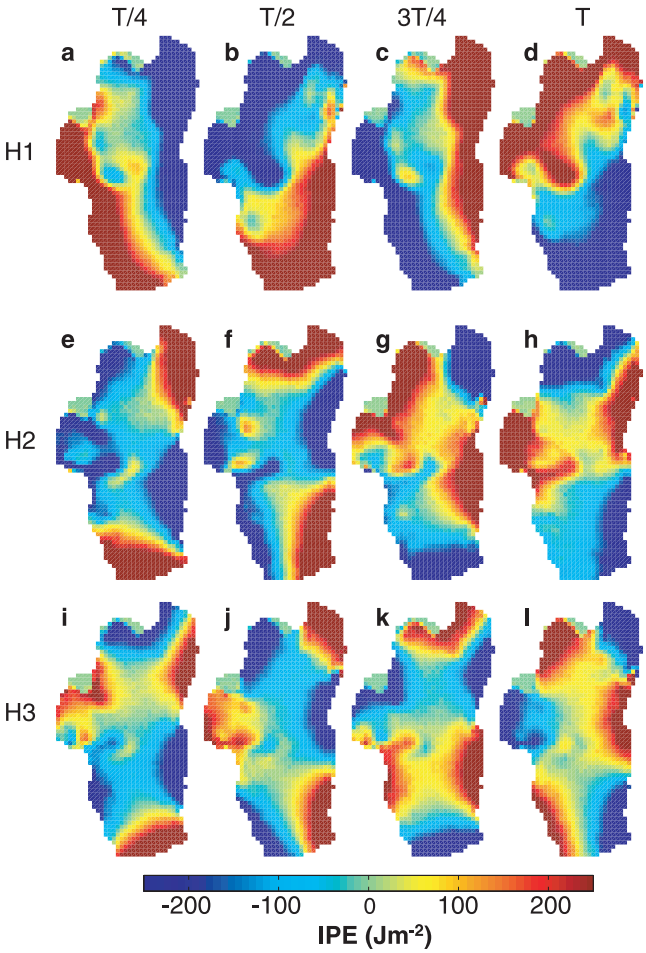

Figure 10. Three modes of Kelvin waves reproduced in the modeled IPE and presented at quarter period intervals. Sense of rotation is cyclonic in all cases. (a–d) First horizontal mode; (e–h) second horizontal mode; (i–l) third horizontal mode. Time series of IPE at each horizontal location are first detrended and then band-pass filtered as specified in Table 2.

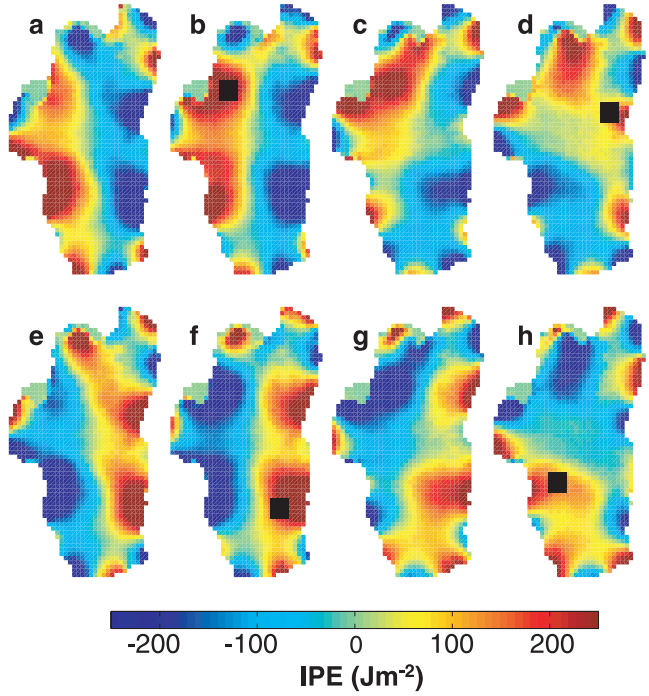

Figure 11. First mode Poincaré wave reproduced in the modeled IPE and presented at 2 h intervals. Sense of rotation is anticyclonic. Wave period is approximately 17 h. Time series of IPE at each horizontal location are processed as indicated in Figure 10. A black box is included to display the clockwise phase propagation of the Poincaré wave.

of plots in Figure 11. Here each plot is separated by 2 h, (slightly less than T/8). It can be clearly seen that the phase propagates anticyclonically around the basin. The behavior of the IPE oscillations in the surrounding embayments, though, does not follow the basin-scale pattern. For example, in Figures 11a and 11b, the wave is causing upwelling in the western shore in the main basin (high positive IPE) while close to the shore in the embayment the IPE signal shows negative values (downwelling). The IPE in the embayment oscillates with a node along the east–west direction, contrary to the general behavior in the main deep basin. The horizontal structure of the oscillations is thus far from being simple. For both the Poincaré mode and the previously discussed Kelvin mode, topographic effects exert considerable influence on the spatial structure of the internal wave field.

[36] A slightly different view of the individual internal wave fields is obtained if one plots the vertical displacement of the 5.5°C isotherm from its equilibrium position. This is shown in Figures 12a–12d for the three Kelvin modes and the Poincaré mode. It is clear from Figure 12 that the high internal wave displacements that are observed are the result of the coincidence of several modes.

5.4. Spatial Structure of IKE Oscillations

[37] The evolution of the IKE field was studied, following the procedures described above for the IPE. The amplitudes, defined as the maximum value in the filtered IKE time series during one selected period, are represented in gray scale surface plots. The time frame studied is day

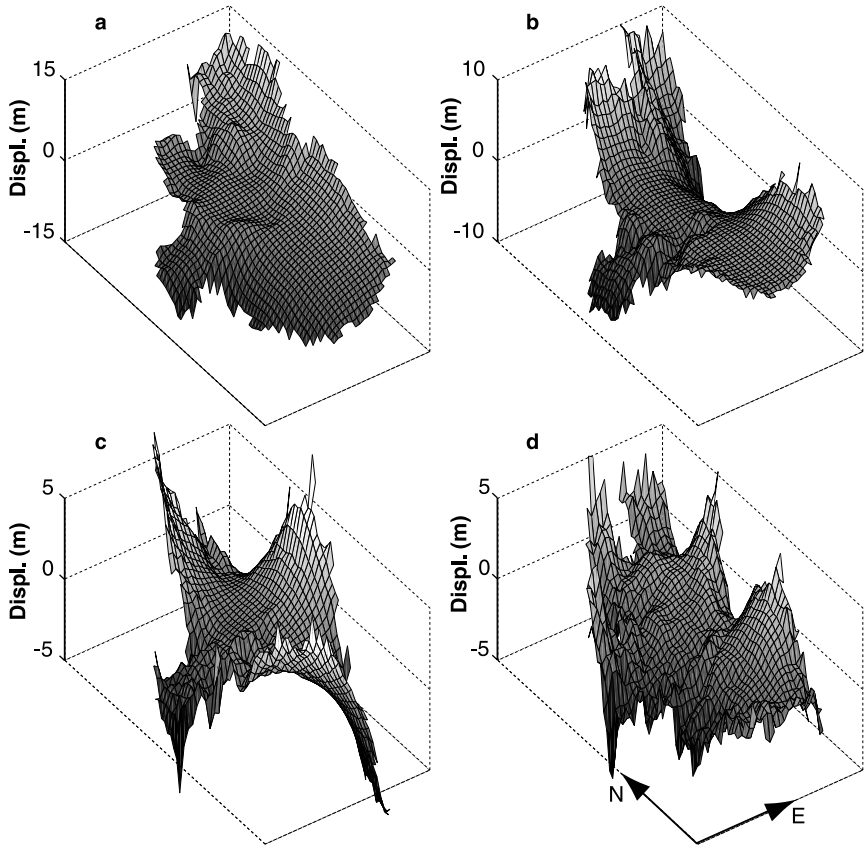

Figure 12. Spatial structure of the 5.5°C isotherm displacement: (a) H1V1 Kelvin wave, (b) H2V1 Kelvin wave, (c) H3V1 Kelvin wave, and (d) H1V1 Poincaré wave. Gray scale gradation corresponds to vertical axis scale in each frame.

350 to 356, 1999 when the agreement between observations and simulations is high. Figure 13 shows the IKE amplitude distribution, for the 17-hour period (Figure 13b) and the 128-hour (Figure 13a) period oscillations. These are the most energetic oscillations observed in the lake. The amplitude of the 128-hour period IKE (Figure 13a) is, in general, highest along the boundaries although regions of increased values projecting from boundaries toward the lake interior (marked in Figure 13a with stars) are present. This pattern repeats itself in higher Kelvin horizontal modes. The regions of high IKE, projecting toward the interior of the lake, coincide with locations where the boundary becomes convex to the cyclonic direction of propagation of the Kelvin wave. Numerical experiments with flat-bottom circular basins, modified to produce convex boundaries, show similar features. The 17-hour oscillations of the IKE field (Figure 13b) exhibit, in general, maximum values at the center. Figure 13b also shows an area of low velocity magnitude along the east–west axis at the center of the lake, which corresponds to a line of low IPE oscillations (see Figure 11).

5.5. Interaction Between the Wind and the Basin-Scale Internal Waves

[38] A well known result in classical mechanics is that the amplitudes of the motions described by a forced harmonic oscillator depend on the energy of the forcing mechanism, the frequency of the forcing compared with the natural

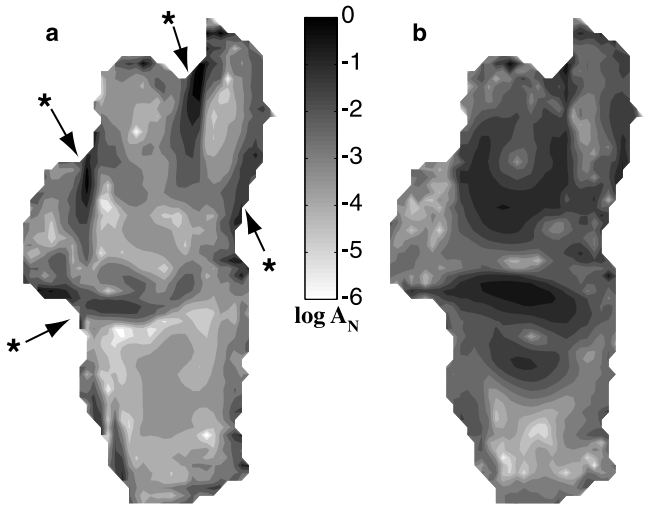

Figure 13. Spatial distribution of the amplitude of IKE oscillations caused by (a) Kelvin wave mode 1 and (b) Poincaré wave. The amplitudes were first normalized using the maximum value in the domain. The natural logarithmic of the normalized amplitude (A_N) is shown using a gray scale. Contours are shown every 0.25 units in the logarithmic scale. Stars mark areas where the high kinetic energy intrude into the interior of the basin.

frequency of the oscillator, and their relative phase [see, e.g., *Wilson*, 1972]. Those concepts are applicable to basin-scale internal waves as shown by *Antenucci et al.* [2000], given that isopycnal oscillations are forced by the wind. *Antenucci et al.* [2000] also presented an analytical model of the response of a two-layer rectangular basin undergoing internal oscillations, with the wind-forcing applied impulsively. In that model, the wind amplifies the signal when a zero relative phase exists. At zero phase, the impulsive force is applied as the wave passes through zero from trough to crest. A relative phase of half the period of the internal wave ($\pm T/2$) results in cancellation of the internal wave energy. This model, although simple, provides insight in the nature of the interaction between the wind applied impulsively on the surface of the lake and the internal waves. Here, the role played by the wind field, in determining the injection-drainage of energy into the internal wave field of Lake Tahoe, is examined by the means of numerical experiments. In particular, the wind phase relative to the phase of the internal wave is investigated. The focus is on two strong wind events with very different effects on the Kelvin wave. The first event commences on day 346 1999, previous to westerly winds of up to 13 m s^{-1}. The inclusion of this event in the simulations proved to be critical in reproducing the large oscillations on days 350 to 360, which points to its role in exciting Kelvin waves. During the second event, on day 355, winds of up to 10 m s^{-1} blew from the east. The wind acts in opposition of phase with the Kelvin wave, which at that time is causing upwelling at the western shore (Figure 2). It is this event that weakens the Kelvin wave in Interval 2 of the simulations. To test this hypothesis, simulations were conducted in which the wind was turned to zero in the momentum equations after day 355 (simulation 1) and after day 357 (simulation 2). The Kelvin wave signal (with a period of 110 hours) was isolated from the simulated IPE time series at the horizontal location (3, 32), next to the INDEX station, using wavelet transforms. Figure 14 shows the amplitude of the Kelvin wave IPE signal for simulations 1 and 2, as well as for the measured wind field. The decay in the Kelvin wave amplitude was measured as the time for it to become half its maximum value (T_d). The decay

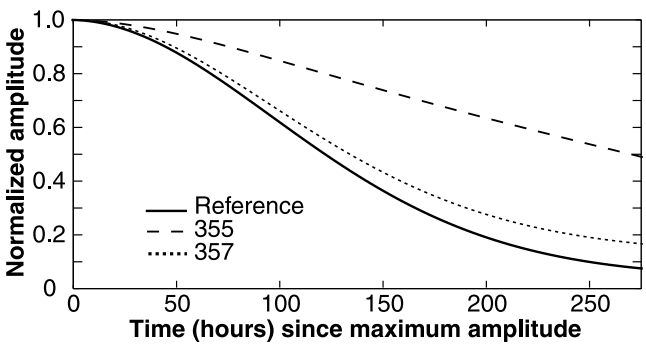

Figure 14. Evolution of the amplitude of simulated IPE signal for the first horizontal mode Kelvin wave (128 h period) at station (3, 32), as calculated through wavelets. The amplitude is normalized using the maximum value in the time series. Reference simulation (solid line) and simulations conducted by removing the wind momentum flux after day 355 (dashed line) and day 357 (dotted line) in 1999.

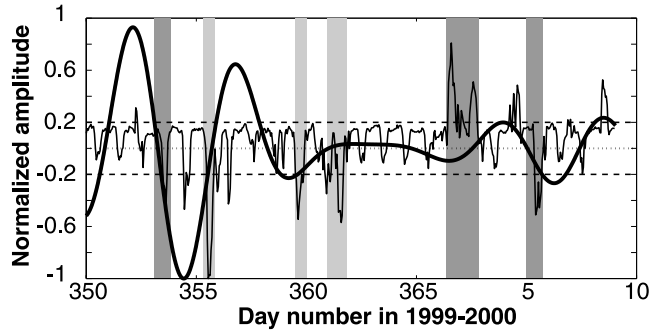

Figure 15. Measured IPE signal at the INDEX station for the first horizontal mode Kelvin wave (as calculated through wavelets) and east–west component of the wind vector. The time series have been normalized using the maximum value during the time window analyzed. Vertical dark shaded bars mark strong wind events when the phase of wind and the Kelvin wave results in the wave being enhanced. Light shaded bars mark events when the interaction is destructive.

in the signal for simulation 2 (T_d = 134 h) is similar to that in the simulation with the true wind field (T_d = 122 h), while for simulation 1 the decay is significantly longer (T_d = 270 h).

[39] The evolution of the amplitude of the Kelvin wave in the observed data can also be studied in relation to the relative phase of the wind and the internal oscillations. The Kelvin wave signal in the observed IPE time series at the INDEX station was extracted from the wavelet transforms and plotted together with the east-west wind component at the USCG weather station (Figure 15). An increase in the IPE time series marks an upwelling at the western shore of the lake, while downwelling periods corresponds to decreasing trends in the series. Easterly winds acting at the time of upwelling will act to energize the internal wave (energizing event), while at the time of downwelling will drain energy from the internal wave (weakening event). In Figure 15 the energizing events are marked with dark shaded bars, while the weakening events are marked with light shaded bars. The decay in the Kelvin wave amplitude follows a series of weakening events, while a series of energizing events precedes the excitation of Kelvin waves at the end of the period under study.

6. Summary and Conclusions

[40] A three-dimensional model for flow and transport in lakes has been used to study the nature of the dominant basin-scale internal waves of Lake Tahoe and their relation to the wind field, under winter conditions. The lake was weakly stratified with a well-defined metalimnion between 50 and 150 m below the free water surface. Despite the weak vertical stratification, the lake was still highly stable with respect to vertical overturn and therefore representative of the conditions that many shallower lakes experience for much of the year. However, the weak stratification, combined with the size of Lake Tahoe, yielded conditions that produced large amplitude internal oscillations with periods approaching 128 hours. Such conditions constitute a very severe test for a numerical model, requiring, in particular,

low levels of numerical dissipation and phase loss, and accuracy in the representation of the turbulent transport.

[41] Four modes of oscillation were isolated in the measured internal wave field, and were positively identified through analysis and display of the model results. Three of the modes have subinertial frequencies and were identified as vertical mode one Kelvin waves traveling cyclonically around the perimeter of the lake with periodicities of approximately 128, 57 and 37 h. The longer period Kelvin wave has horizontal mode 1, while the others have horizontal modes 2 (57 h) and 3 (37 h). The fourth internal wave mode was identified as a vertical mode one, horizontal mode one Poincaré wave having a period of about 17 h, causing transverse oscillations of the isotherms. This is the first time that such a rich array of basin-scale internal wave types has been positively demonstrated to exist in Lake Tahoe, and reinforces similar findings in other medium to large lakes [*Hodges et al.*, 2000; Saggio and *Imberger*, 1998]. The second and third mode Kelvin waves have previously only been observed in considerably larger lakes such as the Great Lakes [*Schwab*, 1977].

[42] Simplified circular models of Lake Tahoe's basin were able to estimate the period of the internal wave modes observed. However, the spatial structure of the wave features cannot be predicted with such tools, particularly in lakes with relatively complex boundaries such as Lake Tahoe. In such cases topographical effects appear to distort the idealized wave structures, and to introduce sub-basin (embayment) oscillations, which appear to exist almost independently of the main basin oscillations. The details of these processes are still not understood, although the effects are clearly evident in the model results.

[43] The numerical experiments and the analysis of IPE records at the INDEX station substantiate the critical role of the relative phase of the wind and the isopycnal oscillations in the decay of the internal wave energy. This has been shown here to be the dominant mechanism of wave dissipation in Lake Tahoe, where storm wind-forcing is not periodic, or at least does not coincide with that of the energetic Kelvin wave. The phase difference between the wind and the internal wave field was seen to be capable of either amplifying the wave energy or annihilating it. While observations and the simulations presented here are similar in the first 10–15 days of the period under study (including a phase of amplification and annihilation), the simulations do not capture the excitation of subinertial waves during Interval 3 at the INDEX station. This could be due to a combination of factors such as (1) numerical diffusion in the momentum equations draining energy from the internal waves, (2) numerical diffusion in the temperature transport equation causing the interface to smear out, (3) the inherent phase error of the numerical algorithm, or (4) the misrepresentation of the relative phase between the wind and the internal waves due to the availability of only a single observation station.

[44] The identification and description of the internal wave field was facilitated by the conjunctive use of both detailed field measurements and a three-dimensional modeling approach. The latter provides spatially intensive information that is not possible to gain with a field measurement program. It also enables one to a posteriori select points of particular interest or importance for analysis. While in the present study the measurements were taken prior to the development of the model, future measurement campaigns will be conducted with the benefit of this tool. It is therefore interesting to consider how a model would best be used. It is evident that for topographically complex lakes, such as Lake Tahoe, the spatial and temporal response of the internal wave field is not straightforward, and the use of simple analytical models to guide instrument placement (as is often done) could miss many of the most interesting features.

[45] We believe that model results can help identify the fewest sampling points that will capture the greatest range of responses, so that in turn the models can be better validated. The lake responses are likely to vary with the strength of the stratification, the vertical location of the stratification with respect to particular bathymetric features, and seasonal changes in wind patterns. Even from year to year, the response of this system is likely to differ, due to the aperiodic interaction of the wind field and the internal wave field. The effects of a single storm were shown to change the internal wave behavior for periods of order 10 days. During certain times (Intervals 1 and 3) the storms increased the internal wave response, while in Interval 2 they were the primary agents in the dissipation of the wave energy. Thus this finite set of sampling points is likely to be inadequate to the task of completely describing the system. The responses are simply too varied, and too changeable. It is only through the combined use of a modeling and informed sampling program can the maximum understanding be gained.

Appendix A

[46] The simplest possible balance in the representation of linear internal wave oscillations is one that invokes the interplay between the inertial and gravity terms [e.g., *Cushman-Roisin*, 1994]

$$\frac{\partial u}{\partial x} + \frac{\partial v}{\partial y} + \frac{\partial w}{\partial z} = 0 \tag{A1}$$

$$\frac{\partial u}{\partial t} + \frac{1}{\rho_0}\frac{\partial p}{\partial x} = 0 \tag{A2}$$

$$\frac{\partial v}{\partial t} + \frac{1}{\rho_0}\frac{\partial p}{\partial y} = 0 \tag{A3}$$

$$\frac{\partial w}{\partial t} - \rho g + \frac{\partial p}{\partial z} = 0 \tag{A4}$$

$$\frac{\partial \rho}{\partial t} + w\frac{\partial \bar{\rho}}{\partial z} = 0 \tag{A5}$$

[47] Assuming a solution of the form $\Theta = \Theta_0 \mathbf{exp}[i(lx + my + nz + \omega t)]$, where Θ represents any of the variables involved in the balance, (l, m, n) are the wave numbers in the x, y and z directions and ω is the frequency of the oscillations, it can be shown that the dispersion relation, linking the frequency and the wave number of such an internal wave is given by

$$\omega^2 = N^2 \frac{l^2 + m^2}{l^2 + m^2 + n^2} \tag{A6}$$

[48] For waves with $l^2 + m^2 \ll n^2$ (i.e. horizontal wavelengths much longer than the vertical wavelengths) the dispersion relation reduces to

$$\omega^2 = N^2 \frac{l^2 + m^2}{n^2} \tag{A7}$$

which is the identical dispersion relation that would be obtained if in equation A4, a balance between the pressure and gravity terms (i.e., hydrostatic balance) were assumed. This is in general the case for basin-scale internal waves. In the particular case of Lake Tahoe, where the basin-scale waves would have a characteristic horizontal length scale of approximately 20 km (the width of the lake) and a vertical dimension of 500 m (the maximum depth), the ratio of vertical to horizontal wavelengths is $O\ (10^{-2})$ and hence $l^2 \sim 10^{-5} n^2$, which justifies the use of an hydrostatic code as a first approach to study such waves.

Appendix B

[49] The model solves Equations 15 and 16, governing the transport of TKE and turbulence macro-scale, using a 3-level fully implicit scheme [*Fletcher*, 1991; *Ferziger and Peric*, 1996]. The variables q^2 and $q^2 l$ are defined at vertical velocity points (interfaces between two cells aligned in the vertical direction). The discretized equations are written as

$$\begin{aligned}
&\frac{3}{2}\frac{(q^2)^{n+1}_{k-1/2}-(q^2)^{n}_{k-1/2}}{\Delta t} - \frac{1}{2}\frac{(q^2)^{n}_{k-1/2}-(q^2)^{n-1}_{k-1/2}}{\Delta t} - \frac{1}{\Delta z^{n+1}_{k+1/2}} \\
&\quad \cdot \left[q^n_{k-1} l^n_{k-1} S_q \left(\frac{(q^2)^{n+1}_{k-3/2}-(q^2)^{n+1}_{k-1/2}}{\Delta z^{n+1}_{k-1}} \right) \right. \\
&\quad \left. - q^n_k l^n_k S_q \left(\frac{(q^2)^{n+1}_{k-1/2}-(q^2)^{n+1}_{k+1/2}}{\Delta z^{n+1}_{k+1}} \right) \right] \\
&\quad = 2A^n_{V_{k-1/2}} \left[\left(\frac{u^n_{k-1} - u^n_k}{\Delta z^{n+1}_{k-1}} \right)^2 + \left(\frac{v^n_{k-1} - v^n_k}{\Delta z^{n+1}_{k-1}} \right)^2 \right] \\
&\quad + 2\frac{g}{\rho_0} D^n_{V_{k-1/2}} \left(\frac{\rho^n_{k-1} - \rho^n_k}{\Delta z^{n+1}_{k-1}} \right) - 2\frac{(q^2)^{n+1}_{k-1/2} q^n_{k-1/2}}{B_1 l^n_{k-1/2}}
\end{aligned} \tag{B1}$$

$$\begin{aligned}
&\frac{3}{2}\frac{(q^2 l)^{n+1}_{k-1/2}-(q^2 l)^{n}_{k-1/2}}{\Delta t} - \frac{1}{2}\frac{(q^2 l)^{n}_{k-1/2}-(q^2 l)^{n-1}_{k-1/2}}{\Delta t} \\
&\quad - \frac{1}{\Delta z^{n+1}_{k+1/2}} \left[q^n_{k-1} l^n_{k-1} S_q \left(\frac{(q^2 l)^{n+1}_{k-3/2}-(q^2 l)^{n+1}_{k-1/2}}{\Delta z^{n+1}_{k-1}} \right) \right. \\
&\quad \left. - q^n_k l^n_k S_q \left(\frac{(q^2 l)^{n+1}_{k-1/2}-(q^2 l)^{n+1}_{k+1/2}}{\Delta z^{n+1}_{k+1}} \right) \right] \\
&\quad = E_1 l^n_{k-1/2} A^n_{V_{k-1/2}} \left[\left(\frac{u^n_{k-1} - u^n_k}{\Delta z^{n+1}_{k-1}} \right)^2 + \left(\frac{v^n_{k-1} - v^n_k}{\Delta z^{n+1}_{k-1}} \right)^2 \right] \\
&\quad + E_1 l^n_{k-1/2} \frac{g}{\rho_0} D^n_{V_{k-1/2}} \left(\frac{\rho^n_{k-1} - \rho^n_k}{\Delta z^{n+1}_{k-1}} \right) \\
&\quad - \frac{(q^2 l)^{n+1}_{k-1/2} q^n_{k-1/2}}{B_1 l^n_{k-1/2}} \left[1 + E_2 \left(\frac{l^n_{k-1/2}}{\kappa z^n_{k-1/2}} \right)^2 \right. \\
&\quad \left. + E_3 \left(\frac{l^n_{k-1/2}}{\kappa \left(H^n - z^n_{k-1/2} \right)} \right)^2 \right]
\end{aligned} \tag{B2}$$

[50] In the leapfrog solution of the momentum equation the eddy coefficients are centered in time, i.e. the eddy viscosity and diffusivity are those calculated for time n. Hence the solution for q^2 and $q^2 l$ at time $n + 1$ is not needed for the calculation of the velocity solution during the initial leapfrog step. The solution for q^2 and $q^2 l$ is obtained after the solution of the momentum and continuity equations with the leapfrog step, and no further iterations are performed. Once q^2 and $q^2 l$ at $n + 1$ have been calculated at the end of the leapfrog step, the eddy viscosity and diffusivity are calculated at $n + 1$ and averaged with the coefficients already calculated for the previous time n, to obtain the eddy coefficients at time $n + 1/2$, that are used in the trapezoidal iterations.

[51] **Acknowledgments.** Logistical support for data collection was provided by Bob Richards of the Tahoe Research Group. This work was collectively supported by the Spanish Ministry of Education and Science, the U.S. Environmental Protection Agency sponsored Center for Ecological Health Research (CEHR) at U.C. Davis, the U.C. Toxic Substances Research and Teaching Program, the Ecotoxicology Lead Campus Program at UC Davis, the National Science Foundation (grant OCE-9906924), and a grant from the U.S. Environmental Protection Agency's Science to Achieve Results (STAR) program. We would like to thank Angelo Saggio for providing scripts to perform spectral density calculations. The constructive criticism of Ben Hodges and an anonymous reviewer helped to improve the manuscript.

References

Antenucci, J. P., and J. Imberger, Energetics of long internal gravity waves in large lakes, *Limnol. Oceanogr.*, *46*(7), 1760–1773, 2001.

Antenucci, J. P., J. Imberger, and A. Saggio, Seasonal evolution of the basin-scale internal wave field in a large stratified lake, *Limnol. Oceanogr.*, *45*(7), 1621–1638, 2000.

Bauer, G., S. Diebels, and K. Hutter, Nonlinear internal waves in ideal rotating basins, *Geophys. Astrophys. Fluid Dyn.*, *78*, 21–46, 1994.

Beletsky, D., and W. P. O'Connor, Numerical simulation of internal Kelvin waves and coastal upwelling fronts, *J. Phys. Oceanogr.*, *27*, 1197–1215, 1997.

Blumberg, A. F., Turbulent mixing processes in lakes, reservoirs and impoundments, in *Physics-Based Modelling of Lakes, Reservoirs and Impoundments*, edited by W. G. Gray, pp. 79–104, Am. Soc. of Civ. Eng., New York, 1986.

Cheng, R. T., T. M. Powell, and T. M. Dillon, Numerical models of wind-driven circulation in lakes, *Appl. Math. Modell.*, *1*, 141–159, 1976.

Csanady, G. T., Large-scale motion in the Great Lakes, *J. Geophys. Res.*, *72*(16), 4151–4162, 1967.

Csanady, G. T., Transverse internal seiches in large oblong lakes and marginal seas, *J. Phys. Oceanogr.*, *3*, 439–447, 1973.

Cushman-Roisin, B., *Introduction to Geophysical Fluid Dynamics*, Prentice-Hall, Old Tappan, N. J., 1994.

Dimai, A., M. Gloor, and A. Wuest, Estimating the intensity of turbulence in the benthic boundary layer of lakes, *Limnologica*, *24*, 339–350, 1994.

Eliason, D. E., and A. J. Bourgeois, Validation of numerical shallow water models for stratified seiches, *Int. J. Numer. Methods Fluids*, *24*, 771–786, 1997.

Ferziger, J. H., and M. Peric, *Computational Methods for Fluid Dynamics*, Springer-Verlag, New York, 1996.

Fletcher, C. A. J., *Computational Techniques for Fluid Dynamics*, Springer-Verlag, New York, 1991.

Fofonoff, N. P., Spectral characteristics of internal waves in the ocean, *Deep Sea Res.*, *16*, 59–71, 1969.

Fricker, P. D., and H. M. Nepf, Bathymetry, stratification, and internal seiche structure, *J. Geophys. Res.*, *105*(C6), 14,237–14,251, 2000.

Galperin, B., L. H. Kantha, S. Hassid, and A. Rosati, A quasi-equilibrium turbulent energy model for geophysical flows, *J. Atmos. Sci.*, *45*(1), 55–62, 1988.

Gardner, J. V., L. A. Mayer, and J. Hughes-Clarke, The bathymetry of Lake Tahoe, California-Nevada, *U. S. Geol. Surv. Open File Rep.*, 98–509, 1998.

Garret, C., and W. Munk, Internal waves in the ocean, *Annu. Rev. Fluid Mech.*, *11*, 339–368, 1979.

Gray, W. G., and D. R. Lynch, Time-stepping schemes for finite element tidal computations, *Adv. Water Resour.*, *1*(2), 83–95, 1979.

Hodges, B. R., J. Imberger, A. Saggio, and K. B. Winters, Modeling basin-scale motions in a stratified lake, *Limnol. Oceanogr.*, *45*(7), 1603–1620, 2000.

Horn, D. A., J. Imberger, and G. N. Ivey, The degeneration of large-scale interfacial gravity waves in lakes, *J. Fluid Mech.*, *434*, 181–207, 2001.

Horn, W., C. H. Mortimer, and D. J. Schwab, Wind-induced internal seiches in Lake Zurich observed and modeled, *Limnol. Oceanogr.*, *31*(6), 1232–1254, 1986.

Hutter, K., Linear gravity waves, Kelvin waves and Poincare waves, theoretical modelling and observations, in *Hydrodynamics of Lakes*, edited by K. Hutter, pp. 39–80, Springer-Verlag, New York, 1984.

Imberger, J., Flux paths in a stratified lake: A review, in *Physical Processes in Lakes and Oceans, Coastal Estuarine Stud.*, vol. 54, edited by J. Imberger, pp. 1–17, AGU, Washington, D. C., 1998.

Imberger, J., and J. C. Patterson, Physical limnology, *Adv. Appl. Mech.*, *27*, 303–475, 1990.

Imboden, D. M., Mixing and transport in lakes: Mechanisms and ecological relevance, in *Large Lakes: Ecological Structure and Function*, edited by M. M. Tilzer and C. Surruya, pp. 47-80, Springer-Verlag, New York, 1990.

Jassby, A. D., C. R. Goldman, J. E. Reuter, and R. C. Richards, Origins and scale dependence of temporal variability in the transparency of Lake Tahoe California-Nevada, *Limnol. Oceanogr.*, *44*, 282–294, 1999.

Kantha, L. H., and C. A. Clayson, An improved mixed layer model for geophysical applications, *J. Geophys. Res.*, *99*(C12), 25,235–25,266, 1994.

Kato, H., and O. M. Phillips, On the penetration of a turbulent layer into stratified fluid, *J. Fluid Mech.*, *37*(4), 643–655, 1969.

Kondo, J., Air-Sea bulk transfer coefficients in diabatic conditions, *Boundary Layer Meteorol.*, *9*, 91–112, 1975.

Kundu, P. J., A numerical investigation of mixed-layer dynamics, *J. Phys. Oceanogr.*, *10*, 220–236, 1980.

Kundu, P. K., *Fluid Mechanics*, Prentice-Hall, Old Tappan, N. J., 1990.

Liu, P. C., and D. J. Schwab, A comparison of methods for estimating u^* from given u_Z and air-sea temperature differences, *J. Geophys. Res.*, *92*(C6), 6488–6494, 1987.

MacIntyre, S., K. M. Flynn, R. Jellison, and J. R. Romero, Boundary mixing and nutrient fluxes in Mono Lake California, *Limnol. Oceanogr.*, *44*(3), 512–529, 1999.

Martin, P. J., Simulation of the mixed layer at OWS November and Papa with several models, *J. Geophys. Res.*, *90*(C1), 903–916, 1985.

Monismith, S. G., Modal response of reservoirs to wind stress, *J. Hydraul. Eng.*, *113*(10), 1290–1306, 1987.

Munnich, M., The influence of bottom topography on internal seiches in stratified media, *Dyn. Atmos. Oceans*, *23*, 257–266, 1996.

Pollard, R. T., P. B. Rhines, and R. O. R. Y. Thompson, The deepening of the wind-mixed layer, *Geophys. Fluid Dyn.*, *3*, 381–404, 1973.

Rosati, A., and K. Miyakoda, A general circulation model for upper ocean simulation, *J. Phys. Oceanogr.*, *18*, 1601–1626, 1988.

Rueda, F. J., A three-dimensional hydrodynamic and transport model for lake environments, Ph.D. dissertation, Univ. of Calif., Davis, 2001.

Rueda, F. J., and S. G. Schladow, Dynamics of a large polymictic lake, part II Numerical simulations, *J. Hydraul. Eng*, in press, 2002.

Saggio, A., and J. Imberger, Internal wave weather in a stratified lake, *Limnol. Oceanogr.*, *43*(8), 1780–1795, 1998.

Schwab, D. J., Internal free oscillations in Lake Ontario, *Limnol. Oceanogr.*, *22*(4), 700–708, 1977.

Schwab, D. J., and D. Beletsky, Propagation of Kelvin waves along irregular coastlines in finite-difference methods, *Adv. Water Resour.*, *22*(3), 239–245, 1998.

Sherman, F. S., J. Imberger, and G. M. Corcos, Turbulence and mixing in stably stratified waters, *Annu. Rev. Fluid Mech.*, *10*, 267–288, 1978.

Smith, P. E., A three-dimensional, finite-difference model for estuarine circulation, Ph.D. dissertation, Univ. of Calif., Davis, 1997.

Thompson, K. L., Winter mixing dynamics and deep mixing in Lake Tahoe, M. S. thesis, Univ. of Calif., Davis, 2000.

Thorpe, S. A., J. M. Keen, R. Jiang, and U. Lemmin, High-frequency internal waves in Lake Geneva, *Philos. Trans. R. Soc. London, Ser. A*, *354*, 237–257, 1996.

Torrence, C., and G. P. Compo, A practical guide to wavelet analysis, *Bull. Am. Meteorol. Soc.*, *79*(1), 61–78, 1997.

Wilson, B. W., Seiches, in *Advances in Hydrosciences*, edited by V. T. Chow, pp. 1–94, Academic, San Diego, Calif., 1972.

F. J. Rueda, S. G. Schladow, and S. Ó. Pálmarsson, Department of Civil and Environmental Engineering, University of California, Davis, CA 95616, USA. (fjr7@cornell.edu)